One-click bending stiffness

Robust and reliable automatic calculation of moment–curvature relation in a cantilever bending test

Broberg, Peter Hede; Lindgaard, Esben; Krogh, Christian; Mosbjerg Jensen, Simon; Gall Trabal, Guillem; Thai, Alexander Fu-My; Bak, Brian Lau Verndal

Published in:
Composites Part B: Engineering

DOI (link to publication from Publisher):
10.1016/j.compositesb.2023.110763

Publication date:
2023

Document Version
Publisher's PDF, also known as Version of record

Composites Part B 260 (2023) 110763

Contents lists available at ScienceDirect

Composites Part B

journal homepage: www.elsevier.com/locate/composites

One-click bending stiffness: Robust and reliable automatic calculation of moment–curvature relation in a cantilever bending test

P.H. Broberg [a,b,*], E. Lindgaard [a,b], C. Krogh [b], S.M. Jensen [a,b], G.G. Trabal [a,b], A.F.-M. Thai [a,b], B.L.V. Bak [a,b]

[a] CraCS Research Group, Aalborg University, Fibigerstræde 16, DK-9220, Aalborg East, Denmark[1]
[b] Department of Materials and Production, Aalborg University, Fibigerstræde 16, DK-9220, Aalborg East, Denmark

ARTICLE INFO

Keywords:
A. Fabrics/textiles
D. Mechanical testing
Bending stiffness
Smoothing spline
Cross-validation

ABSTRACT

The cantilever bending test is one of the simplest and most widely used methods to estimate the bending stiffness of textile materials. A nonlinear moment–curvature relationship can be computed from a single image of a cantilevered textile specimen. However, the calculation of curvature involves second-order differentiation of noisy data, which leads to noise amplification. Traditionally, this is handled by subjectively choosing one of many functions to fit the data or by manual tuning of fitting parameters. The user choices ultimately lead to uncertainties in the data fit. This paper presents a novel automatic data processing method for the cantilever test using smoothing splines with automatic parameter selection through cross-validation. The method is verified on a simulated deflection curve with known bending stiffness and then used to characterise real textile specimens. Finally, the method is validated by simulating the deflection curve using the computed stiffness. This method makes it possible, for the first time, to accurately predict the textile curvature even in the presence of severe noise, without needing user inputs prone to human error. The code used for this paper is freely available with sample data on the repository at https://doi.org/10.5281/zenodo.7376939.

1. Introduction

The stiff and strong behaviour of fibre composite materials makes them attractive in many applications where lightweight structures are desired. This includes the aero-space, automotive, and wind energy industries. The desirable material properties of fibre composites come with the cost of complex manufacturing. To accommodate this, process simulation models may be used to predict the occurrence of manufacturing defects and final fibre orientation of composite parts [1–5]. Simulation of composite manufacturing processes is often done on a macro-scale, assuming homogeneous properties of the textile, to make them computational efficient [6]. The early models neglected the out-of-plane properties of the textiles and primarily focused on the in-plane shear behaviour. However, more recent literature shows that the bending stiffness of textiles plays a huge role in the manufacturing process, especially in the formation and size of wrinkles [7]. It is known that wrinkles may be critical for the structural strength of fibre composite laminates [8,9], which makes the correct characterisation of textile bending stiffness important.

The bending behaviour of textiles is much different from homogeneous materials as the textile structure consists of thin fibres that can move relative to each other. Effectively, this means that textiles subjected to bending kinematically behave very differently than described by classical beam theories, like Bernoulli–Euler and Timoshenko [10]. Despite this, the bending stiffness, B, for textile materials is often defined as the relation between the moment, M, and the curvature, κ, of the textiles' midline, $M = B\kappa$. The effect of transverse loads on the specimen is also often neglected. Classical beam theories define the bending stiffness as $B = EI$, where E is Young's modulus of the material and I is the area moment of inertia. Because of relative fibre movement during textile bending, the macro-scale bending stiffness should be decoupled from the membrane stiffness in textile modelling [11–13]. This means that the bending stiffness needs to be characterised separately. Moreover, textiles typically have a highly nonlinear bending behaviour with higher bending stiffness at lower curvatures [14–16].

Different methods for characterising textile bending stiffnesses have been proposed in the literature. One of the first and most simple

* Corresponding author at: CraCS Research Group, Aalborg University, Fibigerstræde 16, DK-9220, Aalborg East, Denmark.
E-mail addresses: phb@mp.aau.dk (P.H. Broberg), elo@mp.aau.dk (E. Lindgaard), ck@mp.aau.dk (C. Krogh), smj@mp.aau.dk (S.M. Jensen), ggt@mp.aau.dk (G.G. Trabal), afmt@mp.aau.dk (A.F.-M. Thai), brianbak@mp.aau.dk (B.L.V. Bak).
[1] cracs.aau.dk

https://doi.org/10.1016/j.compositesb.2023.110763
Received 29 November 2022; Received in revised form 13 April 2023; Accepted 24 April 2023
Available online 28 April 2023

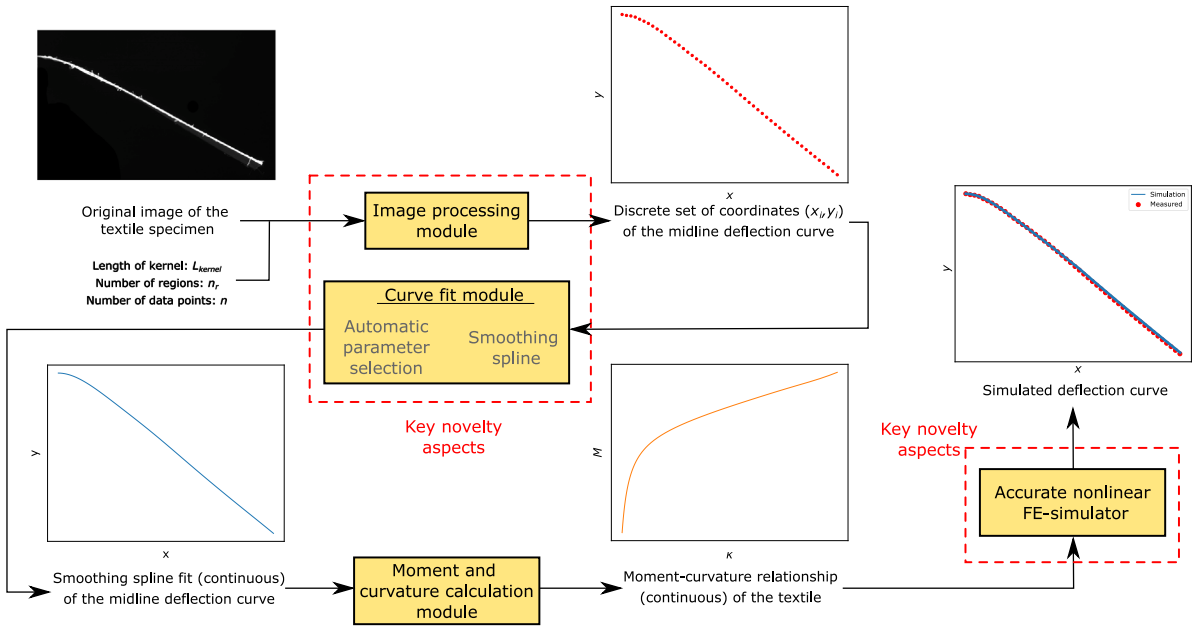

Fig. 1. Overview of the method used for calculating the bending stiffness. The yellow boxes illustrate the modules used for calculations and validation. The key novelty aspects are related to the image processing and the curve fit modules, together with the accurate FE-simulator. (For interpretation of the references to colour in this figure legend, the reader is referred to the web version of this article.)

methods was described by Peirce in 1930 [17]. In this test, a constant bending stiffness of a textile specimen that is cantilevering due to its own weight is estimated. The bending stiffness can be estimated based on the length of the specimen and the angle of an inclined plane passing through the fixed and free end of the specimen. This test is widely used due to its simple setup and data processing, and slightly modified versions of it are also part of ASTM, ISO and British standards [18–20]. The accuracy of the test was improved in [21] by including higher order deformation modes. However, the aforementioned methods assume a linear relationship between the moment and curvature. The Peirce test has since then been the basis for a different kind of test referred to here as the free-hanging cantilever test. In this test, the specimen does not make contact with an inclined plane, but instead an image of the deflected specimen is used to estimate the non-constant bending stiffness. This was first done in 1990 by Clapp et al. [22]. They estimated the non-constant bending stiffness of textiles by fitting a fifth-order polynomial to the deflection curve. More recent literature has further extended this approach. In [23] the nonlinear bending behaviour both during loading and unloading was estimated by taking successive pictures of a cantilevered specimen. More recently in [24], the accuracy of the curvature calculation was improved by fitting a quartic (4th order) B-spline to the deflection curve. Other cantilever methodologies consider the specimen loaded vertically to avoid issues related to twisting of the specimen's free end [25,26]. Another completely different type of bending test measures the moment and curvature directly using a Kawabata testing machine [16]. This has also been done by making a custom-made test rig that fits in a rotational rheometer [27,28]. Other tests include the buckling test [29,30], the 3-point bending test [31–33], and the so-called "free cantilever test" [34] where a strip of textile is hung from its midpoint, i.e. with two deflecting free ends. A comparison of the different bending tests has been carried out in [31,35,36].

In a previous comparison of test setups carried out by the authors [36], all tests showed a fair degree of similarity in the measured bending stiffness. Due to its simple and low-cost setup, as well as its ability to easily adapt to textiles of different bending stiffness, the free hanging cantilever test was considered one of the most promising. The main advantage of using the cantilever bending test is that it is widely accessible due to its minimal investment in equipment [36]. However, the main challenge with this methodology is that differentiation of noisy data is needed for obtaining the curvature of the specimen. There is no consensus in the literature on what function should be fitted to the deflection curve. Clapp et al. [22] use a fifth-order polynomial. Higher order polynomials may be unstable and overfit the data, leading to oscillations. Furthermore, polynomials may also not be able to represent deflection profiles of textiles consisting of piecewise curve shapes as argued by [24]. For these reasons, Liang et al. [24] use a B-spline to fit the deflection curve, i.e. a piecewise polynomial function. However, when using B-splines the user still needs to select spline knots, spline order and smoothing parameters for the least squares fit. These user choices result in uncertainties, which affect the fitted parameters. Ultimately, the computed bending stiffness becomes dependent on the parameters set by the user. In all cases the functions are fitted to the textile's position, even though the desired quantity is the curvature (second derivative). As there is no direct measure of how good the function fits the curvature, the accuracy of the computed bending stiffness can be questioned. That is, low residuals of the position fit do not guarantee a good capture of the curvature.

The aim of this paper is to present an accurate and reliable automatic method for calculating the moment–curvature relation for textiles in a cantilever bending test. The presented method includes a new automatic algorithm for fitting the deflection curve using smoothing splines with automatic parameter selection through cross-validation and a novel image-processing algorithm for filtering out noise in the deflection curve. The method is verified against a deflection curve with known non-constant bending stiffness. The key novelty aspects presented in this paper are:

- A robust, flexible, and fully automatic algorithm for fitting the deflection curve in the cantilever test.
- A new and generally applicable image processing scheme.
- An accurate FE-simulator for validating the computed non-constant bending stiffness.

The rest of the paper is structured as follows: Section 2 describes the method used for processing the image and obtaining the bending stiffness. This includes a presentation of the algorithm used for calculating the smoothing spline and automatically choosing the smoothing

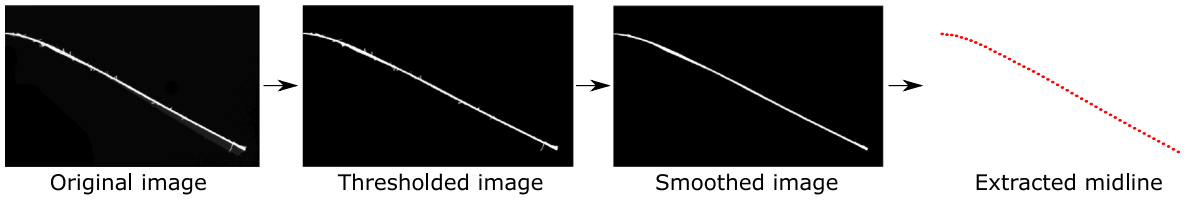

Fig. 2. Three steps are involved in the image processing function: thresholding, smoothing and midline extraction.

parameter through cross-validation. Section 3 presents applications of the code, first on a numerical simulator and subsequently on real test data. Section 4 contains a discussion on the capabilities of the method. Finally, the method and paper are concluded in Section 5.

2. Method of measuring textile curvature and bending stiffness

The workflow of the method for measuring the bending stiffness is illustrated in Fig. 1. The image processing and curve fitting modules have been designed to reduce the number of parameters set by the user compared to earlier published methods [22–24]. The inputs to the program are an image of a cantilevered specimen and three parameters, all with a physical interpretation: the length of the kernel (L_{kernel}) for filtering noise in the thresholded image, the number of regions (n_r) used in the image-processing, and the number of data points (n) extracted from the measured deflection curve. These three parameters are elaborated on in later sections and all have default values that provide accurate and reliable computations for the examples tested in this paper. The *image processing module* converts the raw image to a discrete set of coordinates (x_i, y_i) for the midline deflection curve. To filter out noise, a smoothing spline is fitted to the set of coordinates in the *curve fit module*. The *moment and curvature calculation module* uses the spline fit to calculate the moment and curvature along the specimen length. The output of this program is the nonlinear moment–curvature ($M-\kappa$) relationship for the textile. This method is implemented in a Python program, freely available at https://doi.org/10.5281/zenodo.7376939, and once the raw image is provided, the nonlinear bending characteristic of the textile can be computed with one click.

2.1. Image processing

The image processing module converts the original image to a set of discrete midline deflection values. This is done in three steps: thresholding, smoothing, and midline extraction, see Fig. 2.

During thresholding, the original greyscale image is converted to a binary image using Otsu's method for automatic threshold selection [37]. This method chooses a thresholding value between two peaks in the histogram of the image's greyscale values. For this reason, the input image should have a high contrast between the background and test specimen, and the test specimen should be lighted evenly. More information on this method and implementation in OpenCV (image processing package for python) can be found in [38]. Otsu's method requires no user parameters.

The thresholded image is smoothed to remove noise. As the textile is characterised as a homogeneous material, the noise is related to deviations from the main deflection curve of a prismatic beam. In the investigated experimental data, the primary source of the noise was found to be illuminated loose threads or fibres, see for example the visible white lines emerging from the main deflection curve in Fig. 2. This noise is removed with a morphological opening operation [38] using a line kernel (structuring element) of length L_{kernel} that locally follows the slope of the deflection curve, see Fig. 3. In this step, the slope is estimated automatically by fitting a fifth-order polynomial, $p_5(x)$, to the thresholded image and differentiating it. Two boundary conditions are applied to the fitted polynomial: zero rotation at the

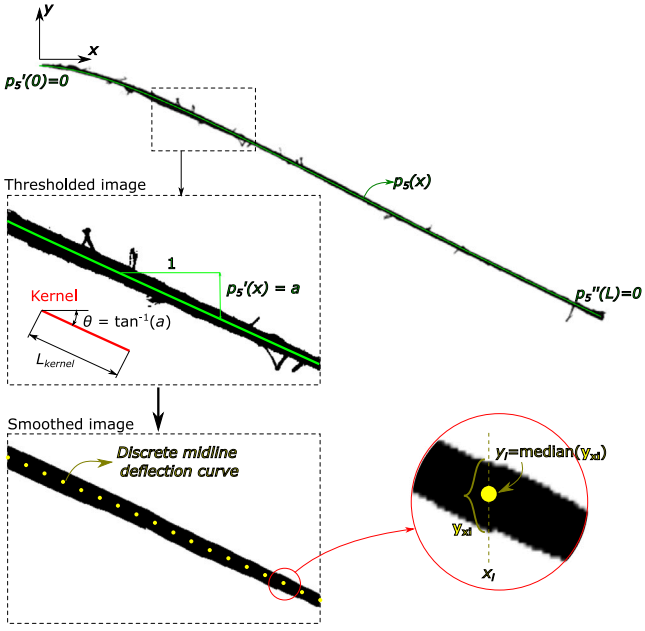

Fig. 3. Method for smoothing the thresholded image. A line kernel following the slope of the deflection curve is used to filter out loose fibres.

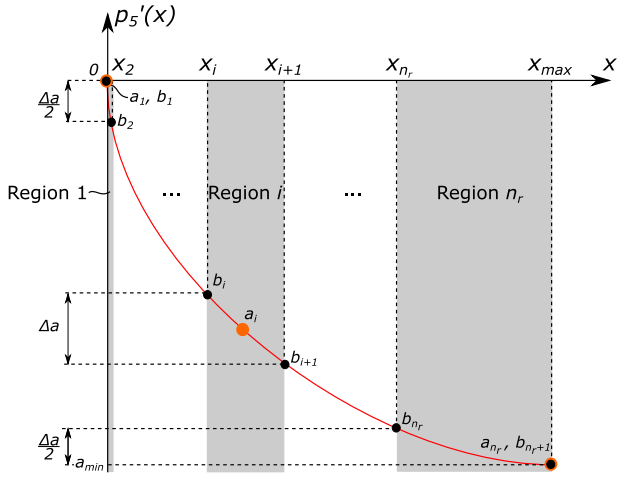

Fig. 4. Definition of region i used during smoothing of the image to estimate the slope θ_i.

fixed end, $p_5^{(1)}(0)=0$, and zero curvature at the free end, $p_5^{(2)}(L)=0$. As the slope is changing continuously along the length of the specimen, the image is divided into n_r horizontal regions ($n_r > 1$) in which the slope can be approximated as constant. This enables the use of a line kernel with a constant slope, a_i, in each region, see Fig. 4. The following method assumes that $p_5^{(1)}(x)$ is monotonically decreasing. The slope of

the line kernel used in region i is defined as,

$$a_i = \Delta a \cdot (i-1), \quad \Delta a = \frac{a_{min}}{n_r - 1}, \quad i = 1, \dots, n_r \tag{1}$$

where a_{min} is the minimum slope of the deflection curve, which is at the free end of the specimen. From the slope, the angle of the line kernel at region i can be found as $\theta_i = \tan^{-1}(a_i)$. Region i is defined on the interval $[x_i;\ x_{i+1}[$ where the boundaries of each region are defined by the slopes, b_i,

$$b_i = \begin{cases} 0 & \text{if } i = 1 \\ a_i - \frac{\Delta a}{2} & \text{if } 2 \le i \le n_r \\ a_{max} & \text{if } i = n_r + 1 \end{cases} \tag{2}$$

from which the spatial boundaries, x_i, are found by solving,

$$p_5^{(1)}(x_i) = b_i, \quad i = 1, \dots, n+1 \tag{3}$$

By this definition, the first boundary is placed at $x_1 = 0$ while the last boundary is placed at $x_{n+1} = x_{max}$. The slopes at all other boundaries are between the slopes of the line kernels, θ_i. In this way, smaller regions are obtained close to the fixed support, which ensures a good representation in regions of large curvature. Two user parameters are needed for this operation: the length of the kernel, L_{kernel}, and the number of regions, n_r. The number of regions should be chosen such that the image is discretised finely enough to represent the continuous change in slope, and the length of the kernel should be chosen such that it is large enough to filter out the loose fibres. The default value of the length of the kernel is $L_{kernel} = 2x_2$, where x_2 is the length of the first region (Fig. 4), and the default value of the number of regions is $n_r = 8$. These values provide effective defeaturing of loose fibres in all the tests presented in this paper. Notice that, the fifth-order polynomial fit of the deflection curve, $p_5(x)$, is only used to choose appropriate settings for the line kernels in the image filtering operation. This should not be confused with the smoothing spline fit that provides a continuous function of the midline deflection for the subsequent curvature calculation.

After the smoothing operation on the thresholded image, the midline of the deflection curve is extracted from the smoothed image, see Fig. 3. The i'th point of the midline deflection, y_i, at x_i is determined as $y_i = \text{median}(\mathbf{y_{xi}})$, where $\mathbf{y_{xi}}$ is a vector containing all y-coordinates for the smoothed image at a given x coordinate, x_i. From the discrete midline deflection curve n data points are picked out by linear sampling and used in the subsequent curve fit. The default value of n is 50 (see Section 3).

2.2. Curve fitting through smoothing splines

The automatic curve fitting algorithm fits a continuous function to the set of discrete coordinates $(x_i,\ y_i)$ of the midline deflection. Smoothing splines are used to filter out the noise left after the image processing. The benefit of using smoothing splines is that they are flexible and can be used to describe a lot of different curves without a priori assumption of the shape. The theory of the equations involved will briefly be covered here. More information on smoothing splines can be found in textbooks, like e.g. [39,40].

The overall idea of smoothing splines is to fit the data points while keeping the m'th derivative low. The $2m-1$ degree smoothing spline, f $(m > 0)$, is given as the minimiser to the function [41,42],

$$\begin{aligned} &\min \quad \sum_{i=1}^{n} \{y_i - f(x_i)\}^2 + \lambda \int \{f^{(m)}(x)\}^2 dx \\ &\text{s.t.} \quad h_k(f) = 0,\ k = 1, \dots, K \end{aligned} \tag{4}$$

The first term in Eq. (4) is the squared difference between data points, y_i, and fitted values, $f(x_i)$, for n number of data points. The second term penalises the m'th derivative of the function f. The parameter λ is the smoothing parameter that determines the level of penalisation.

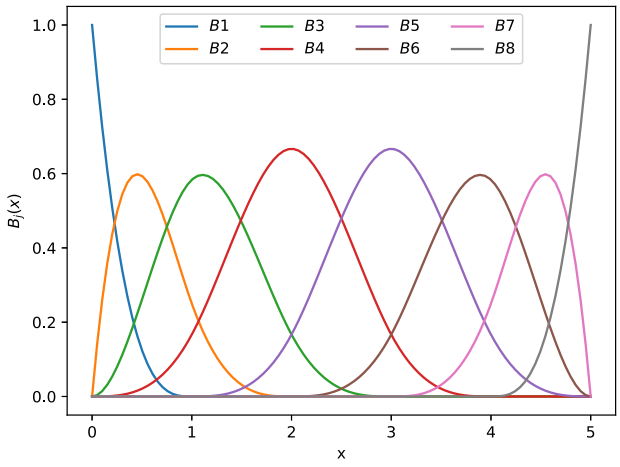

Fig. 5. Basis functions for a cubic spline.

The K number of equality constraints, h_k, which are optional, can be used to impose conditions on the derivatives of the spline. The use of equality constraints, h_k, is elaborated on in the next paragraph.

In the current work, a B-spline basis is used for the smoothing spline, meaning that f in Eq. (4) can be expressed as,

$$f(x) = \sum_{j=1}^{n+2m-2} \gamma_j B_j(x) \tag{5}$$

The parameters γ_j are the linear spline parameters and $B_j(x)$ are the basis functions. The smoothing spline f is, therefore, a linear combination of basis functions $B_j(x)$ of degree $2m-1$. The x values at which the basis functions start and stop are called knots. For smoothing splines, all data points are used as knots, which means that the user does not need to preselect the knots as is the case for regular spline fits. The algorithm used for calculating the basis functions, $B_j(x)$, and the definition of the knot vector will not be described here, but can be found in [39]. An example of cubic $(m = 2)$ basis functions on the data set $x = [0, 1, 2, 3, 4, 5]$ is illustrated in Fig. 5. The k'th equality constraint, h_k, is defined as,

$$h_k(f) = f^{(n_k)}(x_k) - d_k = \sum_{j=1}^{n+2m-2} \{\gamma_j B^{(n_k)}(x_k)\} - d_k \tag{6}$$

Where $f^{(n_k)}(x_k)$ is the n_k'th derivative of f at x_k, and the equality constraint ensures that $f^{(n_k)}(x_k)$ is equal to an arbitrary constant d_k. The Lagrangian function of the problem in Eq. (4), in matrix form, is presented in the following. It can be presented in matrix form because the linear combination of splines in Eq. (5).

$$\begin{aligned} \mathcal{L}(\gamma, \lambda, \zeta) =& (\mathbf{y} - \mathbf{B}\boldsymbol{\gamma})^T (\mathbf{y} - \mathbf{B}\boldsymbol{\gamma}) + \lambda \boldsymbol{\gamma}^T \boldsymbol{\Omega}_B \boldsymbol{\gamma} \\ &+ \zeta^T (\mathbf{C}\boldsymbol{\gamma} - \mathbf{d}) \end{aligned} \tag{7}$$

The matrices $\mathbf{B}$, $\boldsymbol{\Omega}_B$ and $\mathbf{C}$ are given by,

$$\begin{aligned} &\{\mathbf{B}\}_{ij} = B_j(x_i), \quad \{\boldsymbol{\Omega}_B\}_{jk} = \int B_j^{(m)}(t) B_k^{(m)}(t) dt \\ &\{\mathbf{C}\}_{kl} = B_l^{(n_k)}(x_k) \end{aligned} \tag{8}$$

$\mathbf{B}_{ij}$ is a $(n \times (n + 2m - 2))$ matrix with each entry being the j'th basis function evaluated at the i'th data point, x_i. $\{\boldsymbol{\Omega}_B\}_{jk}$ is a $((n + 2m - 2) \times (n + 2m - 2))$ matrix, and can be evaluated efficiently by numerical integration, see [43] for an in-depth description of this. $\mathbf{C}_{kl}$ is a $(K \times (n + 2m - 2))$ matrix with entries being the n_k'th derivative of the l'th basis function at data point x_k, such that $\mathbf{C}\gamma = \mathbf{d}$ where $\mathbf{d}$ is a vector containing the constants d_k.

By using the Karush–Kuhn–Tucker optimality conditions [44], the estimated parameters, $\hat{\gamma}$, that minimises Eq. (7) can be found by solving

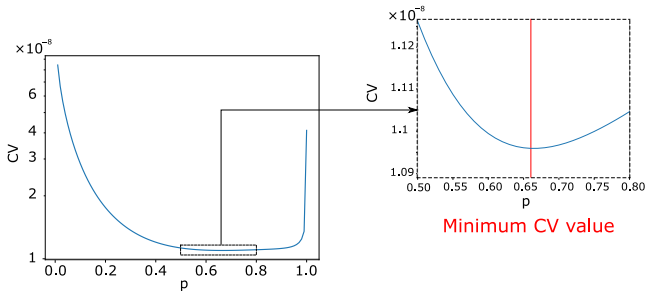

Fig. 6. The smoothing parameter is chosen as the minimiser to the leave-one-out cross-validation value.

the set of linear equations,

$$\begin{bmatrix} 2(\mathbf{B}^T\mathbf{B} + \lambda\boldsymbol{\Omega}_B) & \mathbf{C}^T \\ \mathbf{C} & \mathbf{0} \end{bmatrix} \begin{bmatrix} \hat{\gamma} \\ \zeta \end{bmatrix} = \begin{bmatrix} 2\mathbf{B}^T\mathbf{y} \\ \mathbf{d} \end{bmatrix} \tag{9}$$

Before this system of equations can be solved for the unknown γ and ζ, a selection of constraints, h_k, and calculation of a suited smoothing parameter, λ, are required. The constraints are used to impose physical knowledge on the fit. Textiles behave differently in bending compared to classical homogeneous materials and may be subject to phenomena like e.g. reverse curvature at the free end [14]. To avoid over-constraining, the only constraint added to the fit is, therefore, zero rotation of the specimen at the fixed end, $f^{(1)}(0) = 0$.

The smoothing parameter, λ, is defined on the interval $[0;\ \infty[$. For $\lambda \to 0$ the solution approaches an interpolation on the data points with a spline of degree $2m-1$. For $\lambda \to \infty$ a smooth function with the m'th derivative of f approaching 0 is obtained. A compromise between the bias and variance of the fit is desired in the choice of λ [40]. Bias is an error stemming from a priori assumptions, while variance is an error from sensitivities to small changes in the input data. A fit with high bias tends to underfit/oversimplify the data, while a fit with high variance tends to overfit the data.

The smoothing parameter, λ, is automatically chosen based on the minimisation of the leave-one-out cross-validation, CV, as this provides a trade-off between bias and variance of the fit [40],

$$\min_{\lambda} CV = \frac{1}{N}\sum_{i=1}^{N}(y_i - \hat{f}_{\lambda}^{[-i]}(x_i))^2 \tag{10}$$

$$= \frac{1}{N}\sum_{i=1}^{N}\left(\frac{y_i - \hat{f}_{\lambda}(x_i)}{1 - S_{\lambda}(i,i)}\right)^2 \tag{11}$$

where the notation $\hat{f}_{\lambda}^{[-i]}$ indicates the smoothing spline fit on the data set excluding the i'th data point. $\mathbf{S}_{\lambda}$ is the smoother matrix defined as,

$$\mathbf{S}_{\lambda} = \mathbf{B}(\mathbf{B}^T\mathbf{B} + \lambda\boldsymbol{\Omega}_B)^{-1}\mathbf{B}^T \tag{12}$$

and $\hat{f}_{\lambda}$ is the estimated values of f,

$$\hat{\mathbf{f}}_{\lambda} = \mathbf{S}_{\lambda}\mathbf{y} \tag{13}$$

The cross-validation can be evaluated efficiently for each value of λ once $\mathbf{B}$ and $\boldsymbol{\Omega}_B$ are calculated in Eq. (8).

The smoothing parameter is normalised to avoid evaluating the parameter on an infinitely large interval when finding $\min_{\lambda} CV$ [40,45]. The smoothing parameter λ is, therefore, transformed to the new smoothing parameter p defined on the interval $0 < p \leq 1$. A normalisation based on the *csaps* package for Python [45] is used. In [45] the normalisation of the smoothing parameter for a cubic smoothing spline has been found empirically. In this paper the normalisation is generalised to smoothing splines of an arbitrary degree through a small parameter study.

$$\lambda = k\frac{1-p}{p}, \quad k = 80\frac{\Delta x^{2m-1}}{n^{2m-1}} \tag{14}$$

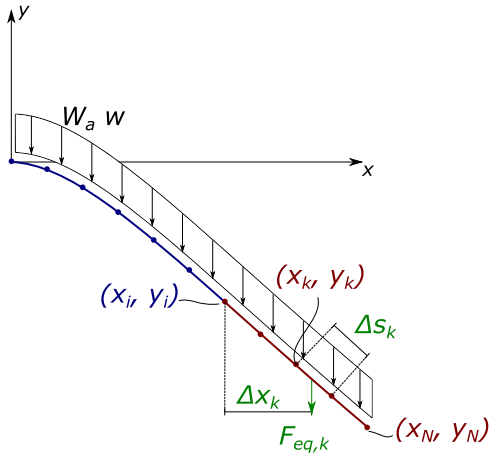

Fig. 7. Illustration of the numerical calculation of the bending moment at the i'th point. The moment contribution from each separate section (between points) are summed up for $x_i < x < x_N$ (red part of the curve). (For interpretation of the references to colour in this figure legend, the reader is referred to the web version of this article.)

$\Delta x = x_n - x_0$ is the span of the x-values. The smoothing parameter is chosen by minimising the CV values between $0 < p \leq 1$, see Fig. 6.

The methodology for curve fitting with B-splines described above is done without any parameter input by the user. A cubic smoothing spline with a penalty on the second derivative ($m = 2$) is often used if the desired fit is on the measured quantity [40]. However, in the case of calculating the curvature of bent textiles, the second derivative of the measured quantity is desired. Therefore, a seventh-degree smoothing spline with a penalty on the fourth derivative ($m = 4$) is used. This means that large changes in the curvature will be penalised in Eq. (4). For a seventh-degree smoothing spline, $p = 1$ gives a spline interpolation of the data, while a curve with linear curvature is fitted on the data for $p \to 0$. All p values in-between represent a flexible function that may provide a good fit while still smoothing out the noise. Again, the smoothing parameter which minimises the CV value provides the best compromise and is chosen in this work to make the approach independent of user settings and interpretations.

2.3. Calculation of moment and curvature

From the spline fit, a continuous description of the deflection curve is obtained, $f(x)$. The curvature at each point can then be determined by [46],

$$\kappa = \frac{-f^{(2)}(x)}{\left(1 + f^{(1)}(x)^2\right)^{\frac{3}{2}}} \tag{15}$$

The superscript to f defines the derivative order. By this definition of curvature and choice of system of coordinates, positive curvature is obtained at the fixed end of the cantilevered specimen. The moment at each point, due to the self-weight of the textile, can be calculated by integration along the arc length of the specimen. A numerical integration scheme is chosen where the moment at each point (x_i) is calculated by (see Fig. 7),

$$M(x_i) = \sum_{k=i}^{N-1} F_{eq,k}\Delta x_k, \quad F_{eq,k} = W_a w \Delta s_k \tag{16}$$

where W_a is the areal weight of the textile, w is the width, and Δs_k is the Euclidean distance between two adjacent points on the deflection curve.

$$\Delta s_k = \sqrt{(x_{k+1} - x_k)^2 + (y_{k+1} - y_k)^2} \tag{17}$$

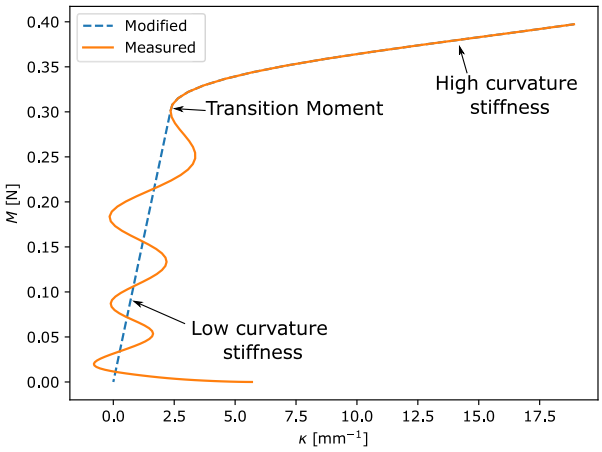

Fig. 8. The $M-\kappa$ curve is modified by assuming a constant bending stiffness at low curvatures to counteract the low curvature oscillations.

Thereby, $F_{eq,k}$ is the equivalent force on the k'th line section. Δx_k is the x-distance from the point at which the moment is calculated, x_i, to the centre point of section k,

$$\Delta x_k = x_k - x_i + \frac{x_{k+1} - x_k}{2} \tag{18}$$

The calculation of the moment at each separate point is illustrated in Fig. 7.

2.4. Modification to control the method in low curvature regions

For some textiles, a classical observation in the computed $M-\kappa$ relationship is oscillations in the low curvature regions [23]. As a remedy to address this issue, the first part of the $M-\kappa$ curve is considered linear up until the last point where the slope of the curve exceeds the secant as shown in Fig. 8. This is done both as this oscillation phenomenon is an artefact of the curve fitting and as a negative slope of the $M-\kappa$ curve would not be usable in some constitutive models. Examples of the oscillations at low curvatures are given in Section 3.1. The $M-\kappa$ curves for the tested textile are approximately bi-linear and can be characterised by the low curvature stiffness, high curvature stiffness and transition moment (see Fig. 8).

2.5. Experimental setup

The experiments are carried out on a simple experimental setup, see Fig. 9. The textile specimen is placed on a box with a level flat top high enough to let the specimen hang freely. A heavy top plate is placed on the specimen to fix it. Spacers with the same thickness as the specimen is placed between the top plate and the box to prevent the weight of the plate pressing down on the specimen, leading to reduced thickness of the specimen which may cause wrong measurements [35]. A monochrome CCD camera is used to acquire images of the side of the specimen, which is illuminated by two NILA Zaila Daylight cool LED white light sources. There should be high contrast between the specimen and the background as mentioned in Section 2.1. Therefore, a black background is chosen to contrast the white glass fibre specimens in Fig. 10. Additional information on the specimen and materials used are presented in Section 3.2. An example of a raw image is shown in Fig. 10.

Care must be taken to prevent systematic errors. The camera must be oriented such that the line of view is perpendicular to the side of the specimen, see Fig. 9. A checkerboard pattern is located in the plane of the specimen's side (Fig. 10) as a sanity check to ensure that the line of view is perpendicular to the specimen [47], and calculate the pixel to metre conversion factor. Furthermore, the box is levelled to ensure

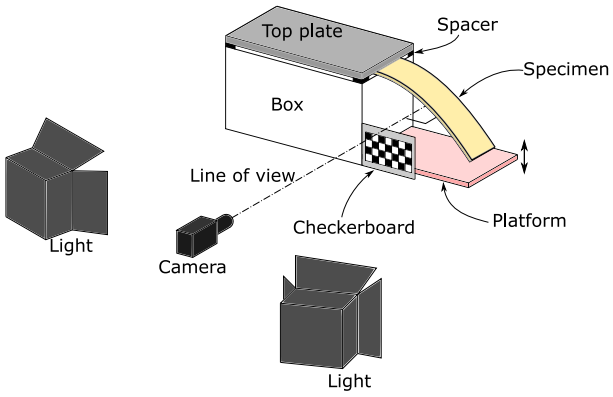

Fig. 9. Experimental setup.

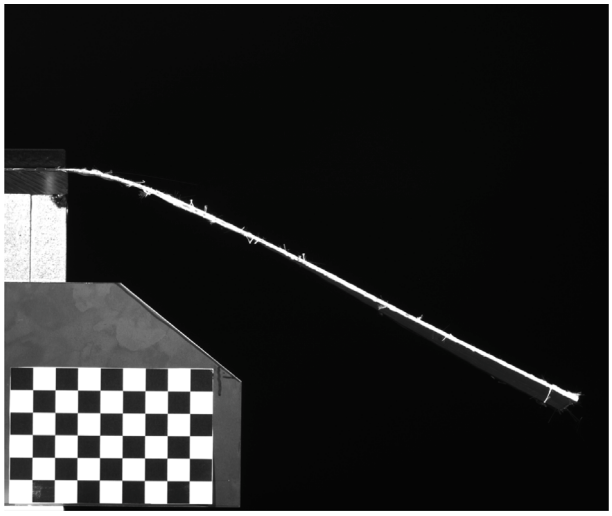

Fig. 10. Example of an image taken during testing. Some twisting of the specimen (grey area) can be observed at the free end of the specimen.

that the gravitational loading acts perpendicular to the undeformed specimen. A moving platform is installed in the setup to ensure that the specimen is not subject to deformation before testing and that the load is applied slowly. Initially, the platform is level with the top of the box and in the course of approximately ten seconds, the platform is lowered until the specimen hangs freely.

The bending stiffness can readily be computed with this raw image of the cantilevered specimen and the three parameters with default values: Length of the kernel, $L_{kernel} = 2x_2$ (where x_2 is the length of the first region, cf. Fig. 4), the number of regions, $n_r = 8$, and the number of data points, $n = 50$.

3. Applications

The measurement errors in the test can be divided into random errors and systematic errors, see Fig. 11. The random errors are noise related to deviations from the midline deflection of a prismatic beam e.g. from buckling of rovings, see Fig. 10, the accuracy of the extraction of the midline by the median value (Fig. 3), and the accuracy of the camera. The systematic errors are differences between the true and average measured quantity. These could for instance be due to perspective of the camera, twist in the specimen, misplacement of the camera, poor illumination of specimens etc. The systematic errors are mitigated by assuring minimal twisting of the specimen and perpendicularity of the camera, while the smoothing spline handles the random errors. In this

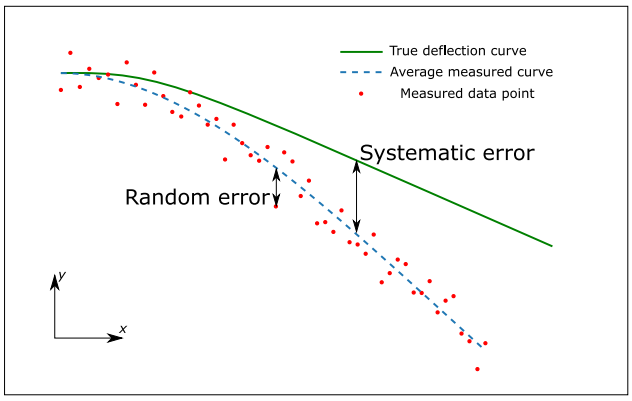

Fig. 11. The measured deflection curve is subject to both random and systematic errors. Systematic errors should be avoided by the experimenter while the random errors are handled by the smoothing spline.

section, it is first verified that the method can compute an accurate bending stiffness from a deflection curve with known non-constant bending stiffness. The method is subsequently validated by computing the bending stiffness from real textile specimens and then using the computed bending stiffness to simulate the deflection curve, see Fig. 12.

3.1. Numerical verification

As a numerical verification, a deflection curve from a beam with a known non-constant bending stiffness is simulated. The purpose of this is to verify that the method, described in the previous section, can represent the correct moment–curvature relationship and to study its sensitivity to noise (random errors), see Fig. 12.

The deflection curve is simulated in an implicit static finite element (FE) analysis framework for geometrically nonlinear analysis using Bernoulli–Euler frame elements with higher order axial terms in a co-rotational formulation [48–50], and a Newton–Raphson solver [51–53]. The finite element analysis framework is modified to introduce a new bending stiffness-curvature relationship. At each load step the curvature in each beam element, κ_i, is calculated by the difference in nodal rotations over the arc length, $\kappa_i = \frac{\Delta\theta}{\Delta_S}$. By assuming that the membrane strains are negligible [23], the Young's modulus of each finite element is calculated from a given input bending-stiffness curvature relationship and the element curvature. The Young's modulus of all finite elements are updated in each increment according to $E_i = B(\kappa_i)/I$. $B(\kappa_i)$ is the bending stiffness as a function of the curvature. For this verification, a representative bending stiffness is chosen to,

$$B(\kappa) = \frac{500}{\kappa^2 + 2000\kappa + 1000} + 0.01 \tag{19}$$

The computed moment–curvature relationship based on the simulated deflection curve is shown in Fig. 13 together with the inputted moment–curvature relationship for comparison. The cross-validation automatically chooses a low level of smoothing (smoothing parameter) as there is no noise in this data. The maximum relative error between the computed and inputted $M - \kappa$ curve in Fig. 13 is 0.77% while the average relative error is 0.26%. Given the small relative errors, the data processing method is verified.

To test the performance of the identification method when subject to noise in the input data, a number of data points are picked out of the deflection curve and normally distributed random noise is added. An example of a simulated data set is shown in Fig. 14. The blue dashed line is the true deflection curve, and the red and green points are data points with normally distributed noise. The simulated test data depends on two parameters: number of data points and amplitude of random noise. The method is tested on four different cases with high/low levels of noise and a high/low number of data points, see Table 1. These data points are inputted directly into the *curve fit module*. The results from the test cases also depend on the seed used in the random number generator, which is the basis for generating the normally distributed noise. For this reason, three sets of noise with different seeds (0, 50, 100 in NumPy [54]) are created.

Table 1
The different test cases for testing the method's sensitivity to noise.

	# data points	Noise amplitude [mm]
Test 1	50	0.1
Test 2	50	1
Test 3	200	0.1
Test 4	200	1

The results for the four test cases with three different noise sets each are shown in Fig. 15. For data with a low amplitude of noise,

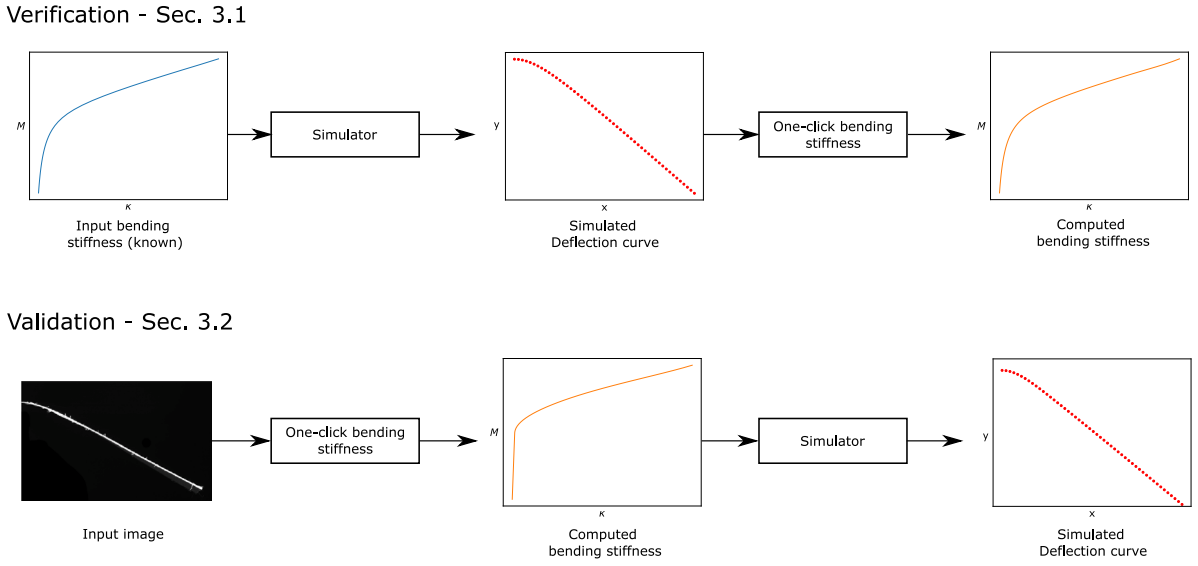

Fig. 12. Flowchart of the verification and validation of the method. The method is verified by comparing the computed bending stiffness from a deflection curve with a known bending stiffness. The validation is done by ensuring that the deflection curve can be represented from the computed bending stiffness from a raw image.

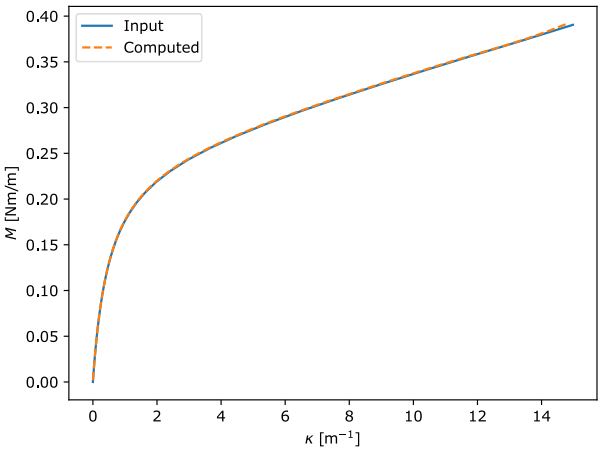

Fig. 13. The input $M-\kappa$ relationship (blue solid curve), and the output $M-\kappa$ relationship from the data processing method on a simulated deflection curve using finite element analysis (dashed orange curve). (For interpretation of the references to colour in this figure legend, the reader is referred to the web version of this article.)

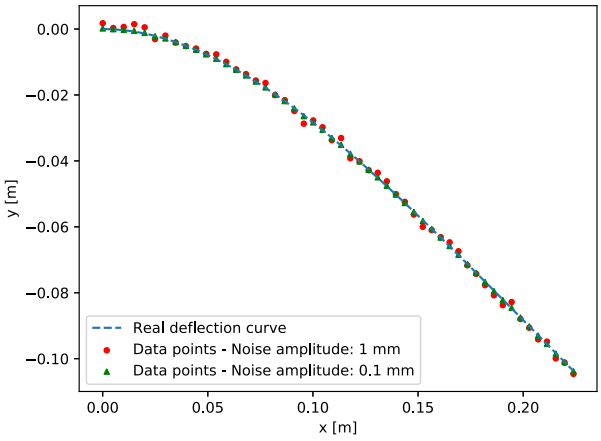

Fig. 14. Example of data points passed into the bending stiffness method. The blue dashed line is the continuous simulated deflection curve, and the red points are the data points with added normally distributed noise. (For interpretation of the references to colour in this figure legend, the reader is referred to the web version of this article.)

the method, generally, gives better representations of the moment–curvature relationship. For the test with a low level of noise and large number of data-points (test 3) all three repeats gives very accurate results. When the noise amplitude increases, accurate results at high curvatures are still obtained while the bending stiffness at lower curvatures, generally, gives less accurate results, and some oscillations. Oscillations at lower curvatures are more pronounced when more data points are used for the fit (test 4).

From these tests it is concluded that this method is capable of accurately representing the moment–curvature relationship when there are low levels of random noise. When the noise amplitude increases, the method still yields accurate bending stiffnesses at higher curvatures, but some oscillations in bending stiffnesses at lower curvatures. The method gives accurate results when using both 50 and 200 data points. However, when 200 data points are included, more oscillations are observed in the computed moment–curvature relationships. The linear approximation of the curve at low curvatures, see Section 2.4, would give a good representation for some of the noise sets (data set 3 in test 2), while it slightly over-predicts the initial linear stiffness for other sets (data set 1 and 2 in test 2). Based on this, accurate computations are obtained by reducing the level of noise by measuring the deflection curve as precisely as possible, and including only sufficiently many data points to represent the deflection curve.

3.2. Characterisation of $M-\kappa$ curve for an UD-NCF

From the previous section it was verified that the method is capable of accurately computing the moment–curvature relationship when subject to random noise. In this section, the method is applied on a quasi uni-directional non-crimp fabric (UD-NCF) to validate that the method are capable of computing a bending stiffness that can be used to accurately simulate the test (Fig. 12).

The UD-NCF textile is a glass fibre NCF with an areal weight of 1380 g/m^2. The layer consists of 96 wt% H-glass fibres with a fibre diameter of 17 to 24 micrometres oriented at 0°. There are 4 wt% E-glass backing fibres with a fibre diameter of 9 micrometres oriented at ±80°. The fibre angles are given relative to the production direction of the textile, see Fig. 16. The stitching is a combined tricot-chain stitch of polyester thread. The specimens have a width of 50 mm and a thickness of approximately 1 mm.

A too small overhang length of the specimen will lead to a small deflection and a poor signal-to-noise ratio, while a too large overhang length will lead to hinge-like behaviour of the specimen close to the fixed end and thus a poor resolution of curvatures. The overhang length of the tested specimens is set to 250 mm, which was found to yield a reasonable compromise. Two configurations of test specimens are investigated: 0° direction with backing side upwards (backing up) and roving side upwards (roving up), respectively. For each case, four repeats of the experiment are carried out with pristine specimens. The specimens hang freely for 2 min before the image is taken to allow them to reach a steady state. Some twisting was observed in the specimens during testing. This twist is due to the architecture of the UD-NCF, see Fig. 10. This twist will cause small changes to the deflection curve in the low curvature region close to the free end. Only the side of the specimen closest to the camera is captured in these experiments, as the effect of twisting is assumed to be negligible. The default values previously specified in Section 2 are used for the image processing: the length of the kernel is chosen as $L_{kernel} = 2x_1$, where x_1 is the length of the first region, the number of segments is chosen as $n_r = 8$, see Fig. 4, and 50 data points are used. For all tests an initial constant bending stiffness up to the transition moment is assumed (Section 2.4).

The results for the test with the roving up can be seen in Fig. 17. It can be observed that there is some variability in the deflection curves for the different specimens. Tests 1 and 3 have similar deflection curves, while tests 2 and 4 have a more stiff response. From the computed bending stiffnesses there are small variabilities. Tests 1, 2 and 4 have a similar low curvature stiffness while test 3 has a slightly lower stiffness at low curvatures. At higher curvatures, test 2, 3, and 4 have a similar stiffness while test 1 has a slightly lower stiffness. Note that, even tough tests 1 and 3 have a similar deflection curve the computed bending stiffness differs, which shows that small difference in deflection can lead to large differences in the computed curvature (second derivative).

Results for the tests with the backing up can be seen in Fig. 18. Like for the other specimen configuration, variability can be observed in the deflection curve and the moment–curvature relationship. The bending stiffness at low curvatures seems to be larger than for the roving up tests and the slope of the moment–curvatures is similar for tests 2, 3, and 4.

The averaged bending stiffnesses for the two tested configurations are shown in Fig. 19. There is a larger variability in the results for the tests on the UD-NCF with the backing up. The slope of the $M-\kappa$ curve is greater for the specimens with the backing up. This applies for both the slope at lower curvatures and at higher curvatures. However, the transition moment is higher for the specimens with the roving up.

3.2.1. Simulation of the deflection curve

To validate the method, the computed bending stiffness is inputted in the finite element analysis framework described in Section 3.1. The results for simulating test 1 of the backing up configuration (blue curve in Fig. 18) are shown in Fig. 20. The maximum and average

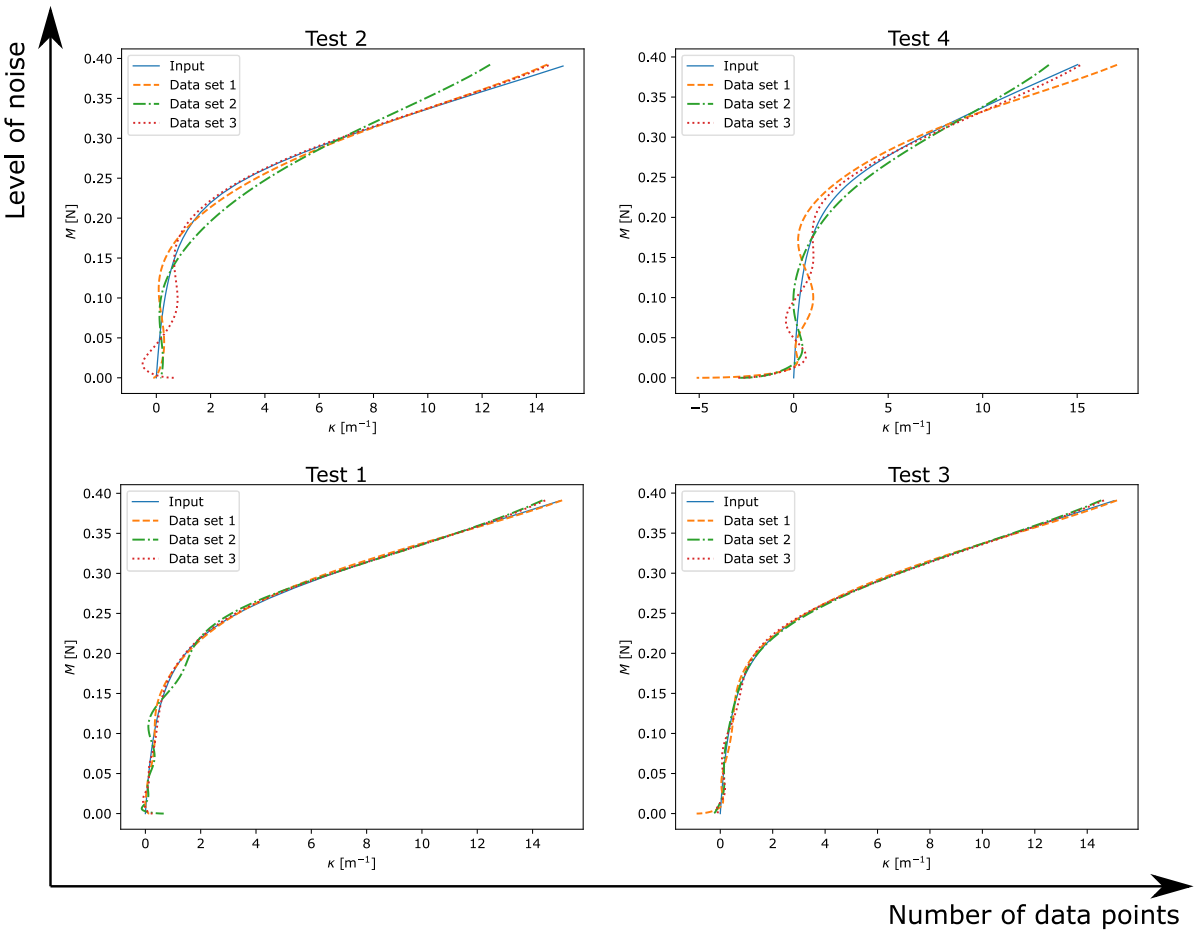

Fig. 15. Resulting $M-\kappa$ relationships obtained using the method on simulated deflection curves with normally distributed noise. The amplitude of the high level of noise is 1 mm while it is 0.1 mm for the low level of noise. Three different simulated deflection curves are tested using three different realisations of random noise added.

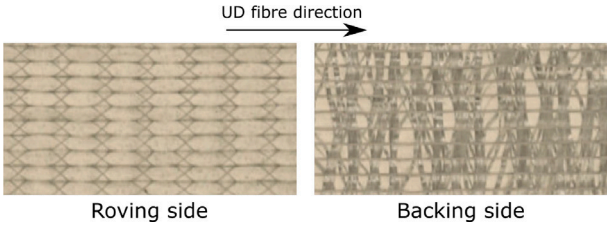

Fig. 16. The tested UD-NCF. Backing side and roving side.

Table 2
Errors between the simulated and measured deflection curves.

	Backing up test 1	Backing up average	Roving up average
Avg. relative	3.33%	1.70%	3.034%
Max relative	63.7%	26.2%	64.9%
Avg. absolute	1.19 mm	0.55 mm	0.48 mm
Max absolute	2.70 mm	3.18 mm	1.79 mm

absolute and relative error between the simulated and the measured deflection curve are listed in Table 2. The maximum relative error is close to the fixed end, where small differences in deflection leads to large relative differences. The maximum absolute error is at the free end. Based on the low average errors between the measured and simulated deflection curves, the simulation accurately represents the deflection curve, especially close to the fixed end where the curvature is largest. Some small discrepancies can be observed closer to the free end with a maximum absolute error of 2.70 mm. The reason for these discrepancies is the use of the linear approximation/modification used at smaller curvatures (see Fig. 8) and due to accumulation of errors along the deflection curve.

The simulated deflection curves using the averaged results from Fig. 19 are shown in Fig. 21. The errors between the simulated deflection curves and the averaged measured curves are listed in Table 2. Again, the maximum relative error is close to the fixed end while the maximum absolute error is at the free end. Using the averaged bending stiffness the deflection curve is in-between the max and the min experimental deflection curve. The simulated deflection curve have a good correlation with the average deflection curve with low average errors. This is both the case for specimens with the backing up and the roving up. Based on the simulation of the deflection curve the entire setup has been validated by using a complicated specimen.

3.2.2. *Influence of camera misalignment on the computed $M-\kappa$ curve*

The effect of systematic errors on the computed $M-\kappa$ relationship is investigated in this section. The most common systematic error anticipated by the authors is misalignment between the camera and the specimen. Ideally, the line of view of the camera should be perpendicular to the specimen to avoid perspective effects, however, this may be difficult to achieve in practice. In the following example, different degrees of misalignment are simulated by applying projective transformation on the image from test 1 with backing up (Fig. 10).

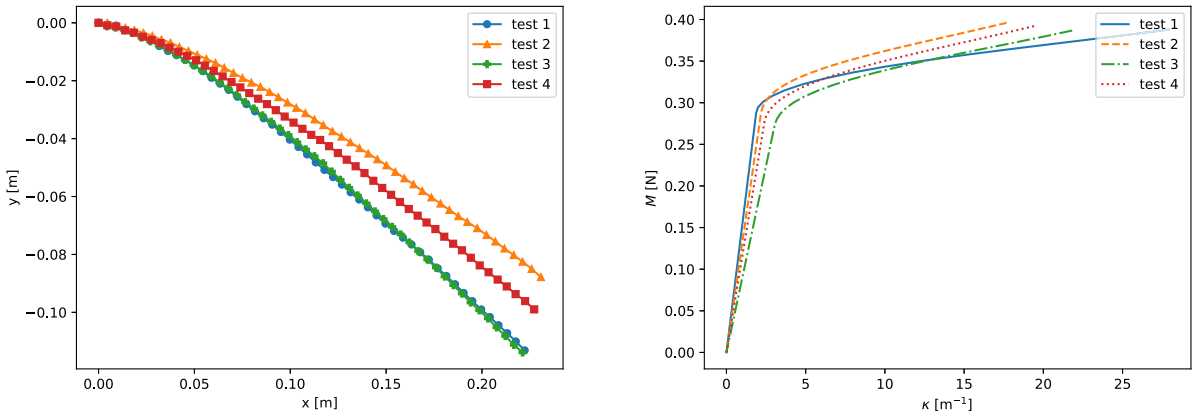

Fig. 17. Test results for the specimens with roving up. Deflection curves for the four specimens after image-processing (left), and computed moment–curvature relationship (right).

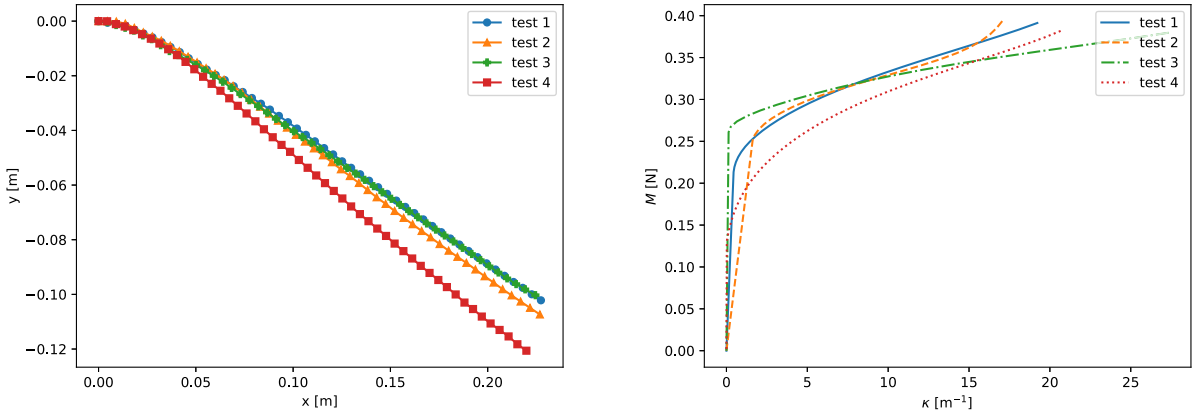

Fig. 18. Test results for the specimens with backing up. Deflection curves for the four specimens (left), and computed moment–curvature relationship (right).

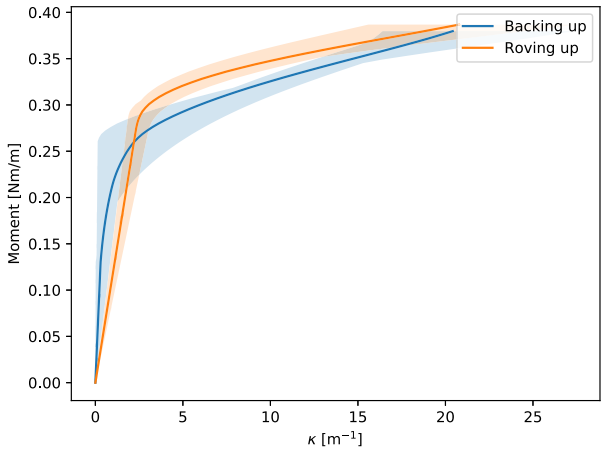

Fig. 19. Averaged $M-\kappa$ relationships for the textile with backing up (blue) and roving up (orange). The shaded blue and orange regions are max and min bands for the computed curves. (For interpretation of the references to colour in this figure legend, the reader is referred to the web version of this article.)

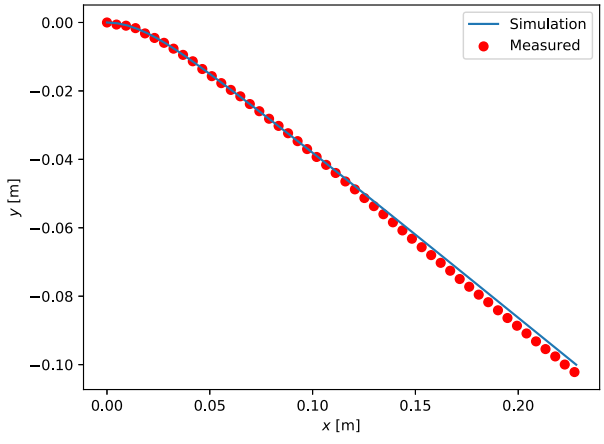

Fig. 20. Simulation of the deflection curve using the computed bending stiffness for test 1 with backing up (blue curve) and the measured curve after image-processing (red dots). (For interpretation of the references to colour in this figure legend, the reader is referred to the web version of this article.)

The projective homography matrix [47] can be found from the relative misalignment and the camera matrix, which is estimated from the focal length of the camera (250 mm). The following four misalignments are considered: 1°, 3°, 5°, and 15°. The distance between the specimen and the camera is 2.5 m. After the image is transformed, it is inputted in the one-click bending stiffness algorithm.

The results are shown in Fig. 22. It can be observed that the computed bending stiffness of the textile decreases as the misalignment increases. The relative difference between the computed bending moment at $\kappa = 10$ m^{-1} for the perpendicular and misplaced image is 0.02% with a misalignment of 1°, −0.62% with a misalignment of 3°, −4.21% with a misalignment of 5°, and −9.98% with a misalignment of 15°. From the deflection curves in Fig. 22 it is observed that the

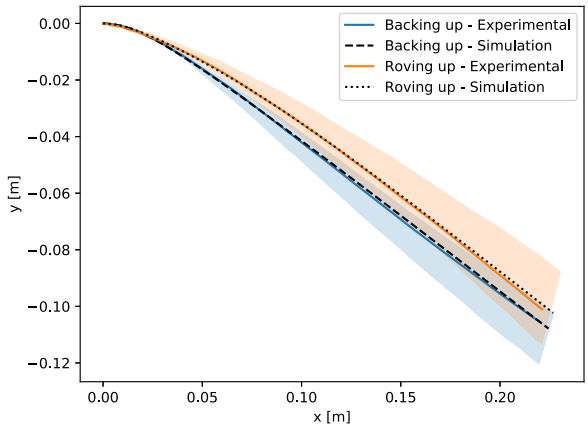

Fig. 21. Simulated deflection curve using the averaged bending stiffness for the tests with roving up and backing up (black dotted and dashed line, respectively), and the averaged deflection curve of the roving up and backing up configuration (orange and blue solid line, respectively). The shaded areas indicate max and min bands for the measured deflection curves. (For interpretation of the references to colour in this figure legend, the reader is referred to the web version of this article.)

length of the test specimens appears shorter with increasing levels of misalignment. This results in reduced bending moments and increased curvatures, which causes the lower computed bending stiffness. To investigate the effect of the decreased bending stiffness, it is inputted in the FE-simulator. The resulting simulated deflection curves are shown in Fig. 23. It can be observed that there is almost no difference in the simulated deflection curve when using the bending stiffness from the perpendicular (original), 1° misalignment, and 3° misalignment image. However, the difference between the deflection curves obtained using the bending stiffness from the perpendicular and 15° misalignment image is significant. It should be noted that the difference in the measured deflection curves (Fig. 22 (left)) not is as big as the difference in the simulated deflection curves (Fig. 23), which highlights the importance of always validating experimental results to ensure that the results are reliable and to detect potential systematic errors.

4. Discussion

The method presented in this paper can compute the bending stiffness of textile materials from a raw image of the cantilevered specimen and three parameters (which all have default values). The method uses a novel smoothing algorithm for removing noise related to deviations from prismatic beams in the image and a smoothing spline with automatic selection of the smoothing parameter to fit the deflection curve. This method enables automatic, objective, and robust computation of the textile moment–curvature relation in the cantilever bending test, which removes the uncertainties and errors arising from subjective user choices in previous methods [22–24]. The end goal of measuring the bending stiffness of textile materials is often to use the measured bending stiffness in a simulation model. In Section 3.2 the computed $M-\kappa$ relationship yielded accurate deflections when inputted in a FE-model of the cantilever bending test. This simple FE-model presents a new and accurate way of validating the measured non-constant bending stiffness by only considering the isolated effect of the nonlinear bending behaviour. Without this thorough validation, the accuracy of the measured bending stiffness (which relies on second derivatives of the curve fit) is questionable. These results demonstrates that the data processing method can handle random errors related to the cantilever bending test. Systematic errors due to e.g. perspective might still be present even though the method is validated by simulation of the deflection curve. The effect of camera misalignment on the computed bending stiffness was investigated in Section 3.2. It was found that small misalignments (1°–3°) have a negligible impact on the computed bending stiffness. Severe misalignments (5°–15°) caused a slight reduction in the computed bending stiffness. However, an easy way to check (and possibly correct) for misalignments is to compare the length of the specimen with the computed length of the deflected specimen. Other systematic errors can be minimised by using a lens without distortion and a large focal length.

The method can readily be used to find the bending stiffness of textile materials from a cantilever bending test. As of now the smoothing parameter, λ, that minimises the leave-one-out cross-validation, CV, is evaluated by choosing the minimum of 100 linearly dispersed CV values on the interval $p =]0;1]$. As the CV function is a simple function that only depends on a single variable, p, on the interval]0;1], this process can be made more efficient by implementing a simple zeroth-order optimisation scheme, like e.g. golden section search [44]. To deal with the oscillations at low curvatures, the $M-\kappa$ curve is assumed linear from (0,0) to the last point where the slope of the curve exceeds the secant from the origin. This method yields reasonable approximations that can be used to accurately simulate the deflection curve. However, if more accurate computations of the bending stiffness at low curvatures are desired another criterion may be defined. This could for instance be to make a linear fit to the low curvatures or include fewer data points close to the free end of the specimen.

The image-processing module, and the moment and curvature calculation module are developed for the specific problem of determining the bending stiffness of cantilevered specimens. However, the implementation of the smoothing spline in the curve fit module is general and may be used in a wide array of applications where derivatives of noisy data are desired. This includes the calculation of bending stiffness in other test setups like e.g. the vertical bending test or the calculation of acceleration from positional data.

The method can be directly applied to cantilever bending test images from other published studies that rely on a high contrast between the test specimen and the background such as [23,24]. Furthermore, deflection curve data obtained in other ways (e.g. by a structured white light scanner [13]) can also be inputted directly in the curve fit module and be processed. The authors encourage the research community to test the new method on their own data to identify potential areas for future research and improvement, and in addition, publish the raw image data of deflected specimens. Ultimately, the authors hope that this work will contribute to the development of more accurate and robust methods for characterising important textile material properties.

5. Conclusion

In this paper, a novel method for determining the non-constant bending stiffness of textiles, with the cantilever bending test, has been proposed. The method can produce the moment–curvature relationship from a single image of the cantilevered specimen. From the raw image, a discrete description of the midline is obtained through thresholding using Otsu's automatic thresholding parameter selection. To remove noise in the image, it is smoothed with a line kernel that follows the slope of the deflection curve. A smoothing spline, with automatic parameter selection using the leave-one-out cross-validation, is used to fit the deflection curve. From the deflection curve and weight of the textile, the moment and curvature at each point can be calculated.

The method was verified against a simulated deflection curve with known bending stiffness and random noise added. It was concluded that the method can successfully represent the correct bending stiffness when small amounts of noise were present. When the amplitude of noise increased, some oscillations occurred in the computed bending stiffness at lower curvatures. These oscillations increased with an increasing number of data points.

Cantilever bending tests on unidirectional non-crimp fabrics were carried out to evaluate the method on real test data. Two experiments were carried out with the backing side up and down, respectively.

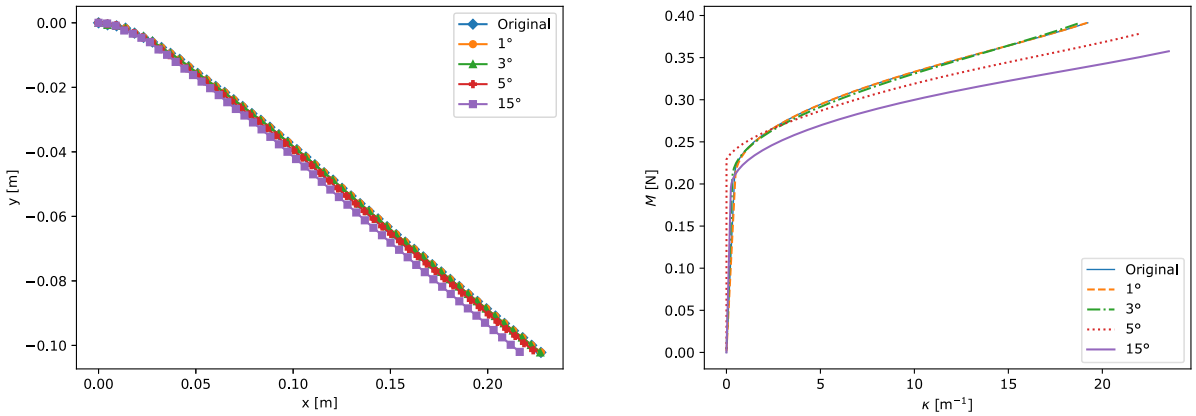

Fig. 22. Results for test 1 backing up considering different camera misalignments. Deflection curves for the four specimens (left), and computed moment–curvature relationship (right).

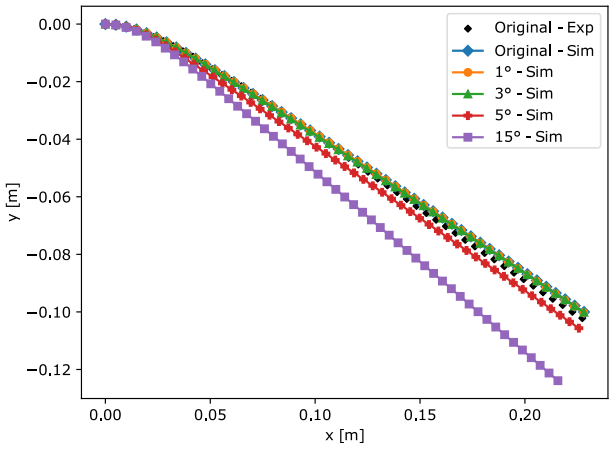

Fig. 23. Simulated deflection curves using the bending stiffness obtained from the images with a misaligned camera.

The method was capable of measuring the non-constant bending stiffness. This was validated by simulating the deflection curve with the computed bending stiffness.

The method minimises the need for user inputs and seeks to eliminate the risk of characterising user-dependent bending stiffness properties by an objective, robust, and automated selection of parameters. The method has been compiled in a freely available Python program readily available at https://doi.org/10.5281/zenodo.7376939 that enables one-click computation of textile bending stiffness, while maintaining the low cost and simplicity of the free hanging cantilever setup.

CRediT authorship contribution statement

P.H. Broberg: Conceptualization, Methodology, Software, Validation, Formal analysis, Investigation, Writing – original draft. **E. Lindgaard:** Conceptualization, Methodology, Investigation, Writing – review & editing, Funding acquisition, Supervision. **C. Krogh:** Conceptualization, Methodology, Software, Investigation, Writing – review & editing. **S.M. Jensen:** Methodology, Software, Writing – review & editing. **G.G. Trabal:** Methodology, Software, Writing – review & editing. **A.F.-M. Thai:** Methodology, Software, Writing – review & editing. **B.L.V. Bak:** Conceptualization, Methodology, Software, Investigation, Writing – review & editing, Funding acquisition, Supervision.

Declaration of competing interest

The authors declare that they have no known competing financial interests or personal relationships that could have appeared to influence the work reported in this paper.

Data availability

I have shared a link to the code with sample data in the manuscript.

Acknowledgements

This study was completed as part of the MADEBLADES research project supported by the Energy Technology Development and Demonstration Program, Grant no. 64019-0514.

References

[1] Potter K, Khan B, Wisnom M, Bell T, Stevens J. Variability, fibre waviness and misalignment in the determination of the properties of composite materials and structures. Composites A 2008;39(9):1343–54. http://dx.doi.org/10.1016/j.compositesa.2008.04.016.

[2] Belnoue J, Nixon-Pearson O, Thompson A, Ivanov D, Potter K, Hallett S. Consolidation-driven defect generation in thick composite parts. J Manuf Sci Eng 2018;140. http://dx.doi.org/10.1115/1.4039555.

[3] Henning F, Kärger L, Dörr D, Schirmaier FJ, Seuffert J, Bernath A. Fast processing and continuous simulation of automotive structural composite components. Compos Sci Technol 2019;171:261–79. http://dx.doi.org/10.1016/j.compscitech.2018.12.007.

[4] Krogh C, Bak BLV, Lindgaard E, Olesen ArM, Hermansen SM, Broberg PH, et al. A simple MATLAB draping code for fiber-reinforced composites with application to optimization of manufacturing process parameters. Structural and Multidisciplinary Optimization; 2021, p. 457–71. http://dx.doi.org/10.1007/s00158-021-02925-z.

[5] Broberg PH, Krogh C, Lindgaard E, Bak BLV. Simulation of wrinkling during forming of binder stabilized UD-NCF preforms in wind turbine blade manufacturing. Key Eng Mater 2022;926:1248–56. http://dx.doi.org/10.4028/p-165q46.

[6] Bussetta P, Correia N. Numerical forming of continuous fibre reinforced composite material: A review. Composites A 2018;113(July):12–31. http://dx.doi.org/10.1016/j.compositesa.2018.07.010.

[7] Boisse P, Hamila N, Vidal-Sallé E, Dumont F. Simulation of wrinkling during textile composite reinforcement forming. Influence of tensile, in-plane shear and bending stiffnesses. Compos Sci Technol 2011;71(5):683–92. http://dx.doi.org/10.1016/j.compscitech.2011.01.011.

[8] Bender J, Hallett S, Lindgaard E. Investigation of the effect of wrinkle features on wind turbine blade sub-structure strength. Compos Struct 2019;218:39–49. http://dx.doi.org/10.1016/j.compstruct.2019.03.026.

[9] Bender J, Hallett S, Lindgaard E. Parametric study of the effect of wrinkle features on the strength of a tapered wind turbine blade sub-structure. Compos Struct 2019;218:120–9. http://dx.doi.org/10.1016/j.compstruct.2019.02.065.

[10] Boisse P, Colmars J, Hamila N, Naouar N, Steer Q. Bending and wrinkling of composite fiber preforms and prepregs. A review and new developments in the draping simulations. Composites B 2018;141(December 2017):234–49. http://dx.doi.org/10.1016/j.compositesb.2017.12.061.

[11] Dörr D, Schirmaier FJ, Henning F, Kärger L. A viscoelastic approach for modeling bending behavior in finite element forming simulation of continuously fiber reinforced composites. Composites A 2017;94:113–23. http://dx.doi.org/10.1016/j.compositesa.2016.11.027.

[12] Thompson AJ, Belnoue JP-H, Hallett SR. Modelling defect formation in textiles during the double diaphragm forming process. Composites B 2020;202:108357. http://dx.doi.org/10.1016/j.compositesb.2020.108357.

[13] Yu F, Chen S, Harper LT, Warrior NA. Simulating the effect of fabric bending stiffness on the wrinkling behaviour of biaxial fabrics during preforming. Composites A 2021;143(August 2020). http://dx.doi.org/10.1016/j.compositesa.2021.106308.

[14] Popper P. Mechanics of bending of fiber assemblies [Ph.D. thesis], 1966.

[15] Grosberg P. The mechanical properties of woven fabrics. Part II: The bending of woven fabrics. Tex Res J 1966;36(3):205–11. http://dx.doi.org/10.1177/004051756603600301.

[16] Lomov S, Verpoest I, Barburski M, Laperre J. Carbon composites based on multiaxial multiply stitched preforms. Part 2. KES-F characterisation of the deformability of the preforms at low loads. Composites A 2003;34(4):359–70. http://dx.doi.org/10.1016/S1359-835X(03)00025-3.

[17] Peirce FT. 26—The "handle" of cloth as a measurable quantity. J Text Inst Trans 1930;21(9):T377–416. http://dx.doi.org/10.1080/19447023008661529.

[18] Standard test method for stiffness of fabrics. 2002, Philadelphia: American Society for Testing and Materials; 2002, [chap.].

[19] Reinforcement fabrics — determination of conventional flexural stiffness — fixed-angle flexometer method. 2011, Geneva, CH: International Organization for Standardization; 2011.

[20] Textiles—test methods for nonwovens—Part 7: determination of bending length. 1998, Standard 1998.

[21] Lammens N, Kersemans M, Luyckx G. Improved accuracy in the determination of flexural rigidity of textile fabrics by the peirce cantilever test (ASTM D1388). Text Res J 2014;84(12):1307–14. http://dx.doi.org/10.1177/0040517514523182.

[22] Clapp TG, Peng H, Ghosh TK, Eischen JW. Indirect measurement of the moment-curvature relationship for fabrics. Text Res J 1990;60(9):525–33. http://dx.doi.org/10.1177/004051759006000906.

[23] de Bilbao E, Soulat D, Hivet G, Gasser A. Experimental study of bending behaviour of reinforcements. Exp Mech 2010;50:333–51. http://dx.doi.org/10.1007/s11340-009-9234-9.

[24] Liang B, Chaudet P, Boisse P. Curvature determination in the bending test of continuous fibre reinforcements. Strain 2017;53(1):e12213. http://dx.doi.org/10.1111/str.12213.

[25] Dangora LM, Mitchell CJ, Sherwood JA. Predictive model for the detection of out-of-plane defects formed during textile-composite manufacture. Composites A 2015;78:102–12. http://dx.doi.org/10.1016/j.compositesa.2015.07.011.

[26] Alshahrani H, Hojjati M. A new test method for the characterization of the bending behavior of textile prepregs. Composites A 2017;97:128–40. http://dx.doi.org/10.1016/j.compositesa.2017.02.027.

[27] Sachs U. Friction and bending in thermoplastic composites forming processes. 2014.

[28] Ropers S, Kardos M, Osswald TA. A thermo-viscoelastic approach for the characterization and modeling of the bending behavior of thermoplastic composites. Composites A 2016;90:22–32. http://dx.doi.org/10.1016/j.compositesa.2016.06.016.

[29] Kocik M, Zurek W, Krucinska I, Geršak J, Jakubczyk J. Evaluating the bending rigidity of flat textiles with the use of an instron tensile tester. Fibres Text East Eur 2005;13(2):31–4.

[30] Wang J, Long AC, Clifford MJ. Experimental measurement and predictive modelling of bending behaviour for viscous unidirectional composite materials. Int J Mater Form 2010;3(SUPPL. 2):1253–66. http://dx.doi.org/10.1007/s12289-009-0670-y.

[31] Ghafour TA, Colmars J, Boisse P. The dahl's model for the inelastic bending behavior of textile composite preforms. Analysis of its influence in draping simulation. Front Mater 2021;8(August):1–16. http://dx.doi.org/10.3389/fmats.2021.728485.

[32] Hübner M, Rocher JE, Allaoui S, Hivet G, Gereke T, Cherif C. Simulation-based investigations on the drape behavior of 3D woven fabrics made of commingled yarns. Int J Mater Form 2016;9(5):591–9. http://dx.doi.org/10.1007/s12289-015-1245-8.

[33] Senner T, Kreissl S, Merklein M, Meinhardt M, Lipp A. Bending of unidirectional non-crimp-fabrics: experimental characterization, constitutive modeling and application in finite element simulation. Prod Eng 2015;9(1):1–10. http://dx.doi.org/10.1007/s11740-014-0568-5.

[34] Mallach A, Härtel F, Heieck F, Fuhr JP, Middendorf P, Gude M. Experimental comparison of a macroscopic draping simulation for dry non-crimp fabric preforming on a complex geometry by means of optical measurement. J Compos Mater 2017;51(16):2363–75. http://dx.doi.org/10.1177/0021998316670477.

[35] Poppe C, Rosenkranz T, Dörr D, Kärger L. Comparative experimental and numerical analysis of bending behaviour of dry and low viscous infiltrated woven fabrics. Composites A 2019;124(December 2018):105466. http://dx.doi.org/10.1016/j.compositesa.2019.05.034.

[36] Krogh C, Broberg PH, Kepler J, Jakobsen J. Comprehending the bending: A comparison of different test setups for measuring the out-of-plane flexural rigidity of a UD fabric. Key Eng Mater 2022;926:1257–67. http://dx.doi.org/10.4028/p-r883x4.

[37] Otsu N. A threshold selection method from gray-level histograms. IEEE Trans Syst Man Cybern 1979;9:62–6. http://dx.doi.org/10.1109/TSMC.1979.4310076.

[38] OpenCV documentation. 2022, https://docs.opencv.org/4.x/index.html. [Accessed 15 August 2022].

[39] Piegl L, Tiller W. The NURBS Book. Springer Series. Monographs in Visual Communication, 1997.

[40] Hastie T, et al. Springer series in statistics the elements of statistical learning. The mathematical intelligencer, vol. 27, no. 2. 2009, p. 83–5, URL http://www.springerlink.com/index/D7X7KX6772HQ2135.pdf.

[41] Schoenberg IJ. Spline functions and the problem of graduation. Proc Natl Acad Sci 1964;52(4):947–50. http://dx.doi.org/10.1073/pnas.52.4.947.

[42] Reinsch CH. Smoothing by spline functions. II. Numer Math 1971;16(5):451–4. http://dx.doi.org/10.1007/BF02169154.

[43] Wand M, Ormerod J. On semiparametric regression with o'sullivan penalized splines. Aust N Z J Stat 2008;50(2):179–98. http://dx.doi.org/10.1111/j.1467-842X.2008.00507.x.

[44] Arora JS. Introduction to optimum design. 4th ed.. (ISBN: 978-0-12-800806-5). Elsevier Academic Press; 2017.

[45] Prilepin E, Husheer S. CSAPS - cubic spline approximation (Smoothing). 2022, URL https://github.com/espdev/csaps/pull/47.

[46] Weisstein E. Curvature, From MathWorld–A Wolfram Web Resource, https://mathworld.wolfram.com/Curvature.html.

[47] Basic concepts of the homography explained with code. 2022, https://docs.opencv.org/3.4/d9/dab/tutorial_homography.html#szeliski. [Accessed13 September 2022].

[48] Crisfield M. Non-linear finite element analysis of solids and structures, vol. 1. John Wiley & Sons Ltd.; 1991.

[49] Cook RD, Malkus DS, Plesha ME, Witt RJ. Concepts and applications of finite element analysis. 4th ed.. John Wiley & Sons; 2002.

[50] Jensen S, Bak B, Lindgaard E, Renart J. Micromechanisms of load history effects in fatigue-driven delamination growth. In: Fagerström M, Catalanotti G, editors. 8th ECCOMAS thematic conference on the mechanical response of composites. 2021, http://dx.doi.org/10.23967/composites.2021.076.

[51] Trabal GG, Bak BLV, Chen B, Lindgaard E. An adaptive floating node based formulation for the analysis of multiple delaminations under quasi-static loading. Composites A 2022;156(January):106846. http://dx.doi.org/10.1016/j.compositesa.2022.106846.

[52] Trabal GG, Bak BLV, Chen B, Carreras L, Lindgaard E. An adaptive floating node based formulation for the analysis of multiple delaminations under high cycle fatigue loading. Composites A 2022;160(June):107036. http://dx.doi.org/10.1016/j.compositesa.2022.107036.

[53] Trabal GG, Bak BLV, Chen B, Jensen SM, Lindgaard E. Delamination toughening of composite laminates using weakening or toughening interlaminar patches to initiate multiple delaminations: A numerical study. Eng Fract Mech 2022;273(August). http://dx.doi.org/10.1016/j.engfracmech.2022.108730.

[54] Harris CR, Millman KJ, van der Walt SJ, Gommers R, Virtanen P, Cournapeau D, et al. Array programming with NumPy. Nature 2020;585(7825):357–62. http://dx.doi.org/10.1038/s41586-020-2649-2.